Can remote sensing combustion phase improve estimates of landscape fire smoke emission rate and composition?

Farrer Owsley-Brown[1,2,3], Martin J. Wooster[1,2,3], Mark J. Grosvenor[1,2,3], Yanan Liu[1,2]

[1]Department of Geography, King's College London, Bush House, 30 Aldwych, London, WC2B 4BG
[2]Leverhulme Centre for Wildfires, Environment and Society, King's College London, London, WC2R 2LS
[3]NERC National Centre for Earth Observation, King's College London, London, WC2R 2LS

Correspondence to: Farrer Owsley-Brown (farrer.owsley-brown@kcl.ac.uk)

Abstract. The proportion of flaming and smoldering activity occurring in landscape fires varies with fuel type and fuel characteristics, which themselves are influenced by ecology, meteorology, time since the last fire etc. The proportion of these combustion phases greatly influences the rate of fuel consumption and smoke emission, along with the chemical composition of the smoke, which influences the effects on the atmosphere. Earth Observation (EO) has long been suggested as a way to remotely map combustion phase, and here we provide the first known attempt at evaluating whether such approaches can lead to the desired improvements in smoke emissions estimation. We use intensively measured laboratory burns to evaluate two EO approaches hypothesized to enable remote determination of combustion phase and concurrent measurements of the smoke to determine how well each is able to improve estimation of smoke emission rates, smoke composition and the overall rate of fuel consumption. The first approach aims to estimate the sub-pixel 'effective fire temperature', which has been suggested to differ between flaming and smoldering combustion, and the second detects the potassium emission line (K-line) believed only to be present during flaming combustion. We find while the fire effective temperature approach can be suited to estimating Fire Radiative Power (FRP), it does not significantly improve on current approaches to estimate smoke chemical makeup and smoke emission. The K-line approach does however provide these improvements when combined with the FRP data, improving the accuracy of the estimated CO_2 emission rate by an average of $17\pm4\%$ and $42\pm15\%$, respectively, depending on whether the K-line detection is used to simply classify the presence of flaming combustion, or whether its magnitude is also used to estimate its relative proportion. Estimates of CO and CH_4 emission rates were improved to a lesser extent than that of CO_2, but the accuracy of the smoke modified combustion efficiency (MCE) estimates increased by $30\pm15\%$ and $46\pm10\%$, respectively. MCE is correlated to the emissions factors

(EFs) of many smoke constituents, so remotely deriving MCE provides a way to tailor these during smoke emissions calculations. Whilst we derived and tested our approaches on laboratory burns, we demonstrate their wider efficacy using airborne EO data of a boreal forest wildfire where we find that combined used of K-line and FRP data significantly change estimated smoke MCE and CO_2 and CO emission rates compared to the standard approach. Our findings suggest that satellite EO methods that jointly provide K-Line and FRP data could enable marked improvements in the mapping of landscape fire combustion phase, fuel consumption and smoke emissions rate and composition.

1. Introduction

Satellite Earth Observation (EO) is the only approach able to provide global, systematic, and regularly repeated estimates of landscape fire trace gas and aerosol emissions (Chuvieco et al., 2019; Wooster et al., 2021). 'Bottom-up' EO-based emissions estimation approaches rely on calculating the amount of biomass burned, based on burned area (BA) or fire radiative energy (FRE) measures (Giglio et al., 2013; Kaiser et al., 2012; Wiedinmyer et al., 2011), which is then multiplied by the emission factor (EF_x) of the chemical species (X) of interest. EF_x represents the mass of that species that is emitted per unit of fuel burned (g kg^{-1}; Andreae and Merlet, 2001). More recently developed EO-based approaches now link EO-derived fire radiative power (FRP) measures directly to emission rates of a trace gas or particulate species via an emission coefficient C_e^X (kg MJ^{-1}; Ichoku and Kaufman, 2005; Mota and Wooster, 2018; Nguyen et al., 2023; Nguyen and Wooster, 2020). However, no EO approach currently takes into account combustion phase and the proportion of flaming and smoldering activity, despite this being known to dramatically influence fire and smoke characteristics (e.g., Freeborn et al., 2008; Urbanski, 2014; Zhang et al., 2015).

The proportion of flaming and smoldering combustion in a landscape fire depends on fuel type and fuel condition – for example being influenced by fuel load, fuel density and fuel moisture content for example (e.g., Burling et al., 2010; Garg et al., 2024; Urbanski, 2013). It is well known that for most chemical species released by landscape burning, the EF_x (and the C_e^x) change markedly between the flaming and smoldering combustion phase (e.g., Reid et al., 2005; Zhang et al., 2015). Therefore, since the proportion of flaming and smoldering combustion varies even between fires burning in the same fuel

type, smoke emissions characteristics can also vary widely – which then has an impact on the fire's effects on atmospheric composition (e.g., Mebust and Cohen, 2013; Zheng et al., 2018).

Biome-specific databases of EF_X and/or C_e^x do not generally report separate values for flaming and smoldering combustion, but rather overall 'fire-averaged' values based on laboratory and/or field measurements assumed to include a 'typical' amount of flaming and smoldering combustion for that fuel type (see Akagi et al., 2011; Andreae, 2019; Andreae and Merlet, 2001). Remote sensing measures of FRP reflect an instantaneous observation, possibly at a time when the amount of flaming and smoldering combustion may be very atypical of the 'average'. Furthermore, even 'fire-averaged' emission factors and coefficients likely vary between fires in the same fuel. For these reasons there is increasing interest in providing more dynamic emission factors and emissions coefficients, initially at least to cope with their presumed seasonal variations (Vernooij et al., 2023, 2022).

There have long been suggestions that remote sensing may be able to provide ways to specify more tailored emissions factors or coefficients (e.g. Andreae and Merlet, 2001; Freeborn et al., 2008; Kaufman et al., 1998). The most common approach suggested uses estimates of sub-pixel fire effective temperature, for example derived via the Dozier (1981) approach or similar multispectral analysis methods that can be used with ground or airborne data (e.g. Dennison et al., 2006) but also with spaceborne data to analyze fires covering only a very small fraction of the pixel area (e.g., Giglio and Kendall, 2001). An alternative approach would be to remotely identify a phenomena characteristic of only a single combustion phase, and most commonly suggested is the potassium line (K-line) radiative emission associated only with flaming activity (Amici et al., 2011; Magidimisha and Griffith, 2017; Vodacek et al., 2002). The current work aims to test these remote sensing approaches to determine whether they really can improve smoke emissions rate and smoke composition estimation, in this case, of the three most dominant trace gases (CO_2, CO and CH_4). We use a series of intensively instrumented combustion chamber burns for this, and also demonstrate the best approaches on real landscape fires using airborne EO data – providing a demonstration that is of intermediate scale to satellite EO.

2. Background

Though the burning of biomass involves multiple different combustion phases, almost all the smoke is produced in the flaming and smoldering phases (Bertschi et al., 2003; Yokelson et al., 1997). The flaming phase generally involves higher temperatures, and the resulting oxidation of fuel carbon is typically far more complete and leads to a higher CO_2 emission factor (Zhang et al., 2015). EFs of species such as NO_X, SO_2 and black carbon (BC) are also elevated in the flaming phase (Andreae and Merlet, 2001; Reid et al., 2005). Smoldering combustion commonly refers to a combination of pyrolysis (thermal decomposition of the fuel) and glowing combustion (of char), mostly involving lower temperatures and more incomplete oxidation of the fuel carbon compared to flaming. CO_2 EFs are lower, but those of species such as CO, CH_4, organic carbon (OC), and volatile organic compounds (VOCs) are higher (e.g. Zhang et al., 2015; Andreae, 2019; Bertschi et al., 2003; Reid et al., 2005; Yokelson et al., 1997, 1996). However, fuel combustion rate is also important to consider in emissions rate calculations, and is far higher per unit area for flaming rather than smoldering combustion (e.g., Lacaux et al., 1996; Wooster et al., 2011) . Furthermore, despite EF_{CO2} being typically 5-15% lower for smoldering than flaming combustion, smoldering fires still release the majority of their carbon as CO_2 as the emissions factor of CO_2 is still higher than for any other compound (e.g., Reisen et al., 2018; Zhang et al., 2015). However, the EF of 'preferentially smoldering' compounds such as CO, CH_4, organic carbon (OC), and VOCs are typically many times higher during smoldering than flaming phase combustion, so along with the fuel consumption rate the amount of smoldering activity plays a very significant influence in their emission rate.

Whilst landscape fires often show periods of only smoldering combustion, periods of 'flaming-dominated' activity are, typically, relatively short. Far more common are stages with a mixed contribution, where some smoldering is happening behind the flaming front (e.g., Bertschi et al., 2003; Burling et al., 2011; Rabelo et al., 2004; Urbanski, 2014; Yokelson et al., 1997). Since combustion rate per unit area is generally far higher in the flaming-dominated phase than the smoldering-dominated phase, the total production of even 'preferentially smoldering' species can often be higher during the flaming period rather than during pure smoldering, depending on the area affected by each and their relative durations. This complexity has led to metrics like the modified combustion efficiency (MCE), which aims to quantify the balance between flaming and smoldering combustion in the smoke production process, defined as:

$$MCE = \frac{\Delta CO_2}{\Delta CO_2 + \Delta CO} \tag{1}$$

where ΔX indicates the excess concentration of CO_2 or CO (commonly measured in ppmv).

Purely flaming combustion results in an MCE close to 1.0 due to minimal CO production, whilst purely smoldering combustion can yield smoke with an MCE as low as 0.65 (depending on fuel type; Akagi et al., 2011; Andreae, 2019). Smoke MCE has been shown to be negatively correlated with the EFs of many preferentially smoldering species (Bertschi et al., 2003; McMeeking et al., 2009; Urbanski, 2013; Yokelson et al., 1996), and understanding the MCE of the fire can therefore enable more precision to be placed on the resulting fire emissions. However, collecting MCE data on landscape fires is challenging even using *in situ* aircraft sampling due to atmospheric mixing (Yokelson et al., 2013), and whilst satellite EO has shown an ability to probe smoke emissions ratios (e.g., Coheur et al., 2009; Ross et al., 2013) it has not yet been possible to remotely sense smoke MCE. Currently, therefore, remote sensing approaches potentially able to determine the amounts of flaming and smoldering combustion ongoing in a fire are based either on retrieving the fire's effective temperature (e.g., Zhukov et al., 2006) or detection of the flaming-phase K-line signature (e.g., Amici et al., 2011).

Remotely sensed fire effective temperature estimation was first proposed by Dozier (1981). Observations in two different wavebands are used to retrieve a fire's subpixel effective temperature (T_r) and proportional area (p), with the fire assumed to be thermally homogeneous and superimposed on a thermally homogeneous background with temperature (T_b) and proportional area ($1-p$). Blackbody behavior is generally assumed, and estimation of T_r and p is conducted via solution of:

$$L_1 = \tau_1 p B(\lambda_1, T_r) + (1-p) L_{b,1} + L_{atm,1} \tag{2}$$

$$L_2 = \tau_2 p B(\lambda_2, T_r) + (1-p) L_{b,2} + L_{atm,2} \tag{3}$$

where L_1 and L_2 are spectral radiances ($Wm^{-2}sr^{-1}m^{-1}$) in wavebands λ_1 and λ_2, τ_1 and τ_2 are the atmospheric transmittances in those wavebands, and $L_{atm,1}$ and $L_{atm,2}$ are the atmospherically emitted radiances measured by the sensor in those wavebands. $L_{b,1}$ and $L_{b,2}$ are the radiance contributions from the non-burning uniform background, whose temperature is generally estimated from neighboring pixels. The spectral emission at wavelength λ and retrieved temperature T_r is given by Planck's Radiation Law:

$$B(\lambda, Tr) = \frac{2hc^2}{\lambda^5} \frac{1}{e^{\frac{hc}{\lambda k_B Tr}} - 1} \tag{4}$$

where h is Planck's constant ($6.62607004 \times 10^{-34}$ kgm^{2}s^{-1}), k_B is Boltzmann's constant ($1.38064852 \times 10^{-23}$ kgm^{2}s^{-2}K^{-1}) and c the velocity of light in a vacuum (299792458 ms^{-1}). Note that "effective temperature" refers to an estimate of the radiant temperature of the fire, rather than the kinetic temperature one might measure with a thermometer. This assumes that the fire is a grey body (Johnston et al., 2014) but makes no assumptions with regards to the actual emissivity value.

120 Dennison et al. (2006), Dennison and Matheson (2011); Matheson and Dennison (2012), Zhukov et al. (2006) provide examples of mapping sub-pixel fire effective temperature, which can be expanded to estimate increased thermal component fits if more than two wavebands are available, such as in hyperspectral data (Dennison et al., 2006; Dennison and Matheson, 2011; Giglio and Justice, 2003; Giglio and Kendall, 2001; Waigl et al., 2019). This could potentially determine separate flaming and smoldering contributions. However, no studies have yet linked such retrievals to an ability to better estimate
125 smoke emission characteristics (Wooster et al., 2021), despite that being a key aim for such data.

The alternative K-line approach is based on the detection of an emission doublet in the near infrared (766.5 nm and 769.9 nm), which is caused by thermally excited potassium atoms within the burning fuel (Vodacek et al., 2002; Amici et al., 2011; Dennison and Roberts, 2009; Magidimisha et al., 2023; Magidimisha and Griffith, 2017). Only flaming phase activity is hot enough to produce K-line emission and Amici et al. (2011) thus far provide its only detection from space – defining the
130 'Advanced K Band Difference' (AKBD) metric to quantify its strength:

$$\text{AKBD} = \text{Max}|\text{BandK}_i| - \text{Bkg} \qquad (5)$$

where $\text{Max}|\text{BandK}_i|$ is the maximum spectral radiance recorded in the 764 nm – 772 nm range (the region that encompasses the NIR K-line doublet) and Bkg is that recorded just outside the K-emission region, for example 779nm. The K-line signature can be seen superimposed on the background Planckian signal in data from our experiment shown in Fig. 2a.

3. Laboratory experiment method

135 **3.1 Experiment setup**

Experiments were conducted at King's College London's Wildfire Testing Chamber, located at Rothamsted Research, Harpenden (UK). The physical arrangement and instruments are detailed in Fig. 1 and Table 1. The remote sensing instruments were positioned to view the fuel-bed at nadir (location B in Fig. 1) through appropriately transparent windows

(also listed in Table 1) with high heat resistance. Pre-experiment calibrations were undertaken to allow the non-unitary

140   transmissivity of the windows to be taken account of during data analysis.
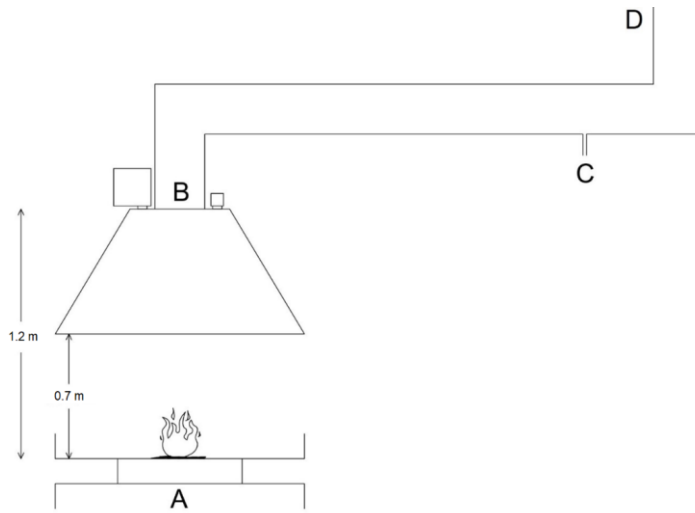
Figure 1. Experimental setup for examining fire and smoke characteristics: (A) Fuel-bed; (B) Spectrometers and cameras viewing the fuel-bed and nadir through holes in the extraction flue; (C) Gas analyzers, (D) Air flow rate sensor.

145

Table 1. Instruments used and their specifications, as well as the window compositions that protected the spectrometers and cameras viewing through the holes shown in Fig. 1.

Location	Instrument	Window	Specifications
A	Digital Scales	NA	0.005 kg readability

B	VIS-SWIR spectrometer - SVC HR-1024i	Sapphire (AL$_2$O$_3$)	Spectral Range: 350 nm – 2500 nm FWHM: 3.5 nm (700 nm), 9.5 nm (1500 nm), 6.5 nm (2100 nm) Bandwidth: 1.5nm (350 nm – 1000 nm), 3.8 nm (1000 nm – 1890 nm), 2.5 nm (1890 nm – 2500 nm) FOV: 14° foreoptic lens Calibration Accuracy: ±5% (400 nm), ±4% (700 nm), ±7% (2000 nm) Measurement frequency: 0.14 – 0.25 Hz
B	Thermal camera - Optris PI 400	Zinc Selenide (ZnSe)	Spectral Range: 7.5 µm – 13 µm Optical Resolution: 382 x 288 pixels Framerate: 27 Hz Temperature Range: 150 °C – 900 °C FOV: 62° x 49° f = 8 mm Measurement frequency: 1 Hz
B	UV-NIR spectrometer - Ocean Insight OCEAN-HDX-XR	Fused silica (SiO$_2$)	Spectral Range: 200 nm – 1100 nm FWHM: 1.1 nm FOV: 30° fiber-optic guide Measurement frequency: 1 Hz
B	RGB camera - Apeman A79	Fused silica (SiO$_2$)	Resolution: 20 MP Framerate: 30 fps FOV: 170°

C	CO_2, CO and CH$_4$ analyzer - Los Gatos Research Ultraportable Emissions Analyzer	NA	CO_2: 0 – 3000 ppm CO: 0 – 1000 ppm CH_4: 0 – 100 ppm H_2O: 0 – 99% relative humidity Measurement frequency: 1 Hz
C	CO_2 and CO analyzer - GasLab CM-1000	NA	CO_2: 0 – 10000 ppm CO: 0 – 5000 ppm Measurement frequency: 0.5 Hz
D	Air pressure differential analyzer - Testo 440	NA	Pressure differential measuring range: -150 hPa to 150 hPa Accuracy: ±0.2 hPa Resolution: 0.01 hPa Measurement frequency: 1 Hz

3.2 Fuel

Three types of fuel were burned during these experiments: oak kindling, pine forest litter, and soybean crop residue. Oak kindling was selected for its relative uniformity, though the thickness and dryness of the individual pieces was not identical and led to some intra-fire variability in the amount of flaming and smoldering activity. The pine forest litter was a mixture of needles, cones and small branches collected from the floor of a UK forest containing mainly Corsican, Maritime, and Scots pine. This fuel mix was dried indoors for a month prior to the burns and the samples burned were selected to maintain the proportions of needles, cones, and branches found on the forest floor. The soybean residues were sourced from China as an example of an agricultural waste product commonly burned in open fields. All fuels were arranged to fit within a 29 cm diameter circle to fit within the measurement area of all remote sensing instruments deployed.

3.3 Fire measurements

3.3.1 Optical and thermal imagery

A standard RBG camera recorded video imagery of each fire for context, helping gauge how amounts of flaming and smoldering combustion changed over each fire's duration. A calibrated longwave infrared (LWIR) camera (Optris PI400) recorded infrared brightness temperature imagery at 1 Hz, with the 3.3 mm pixel size allowing for an assumption of pixel thermal homogeneity. A 1 Hz FRP record of the fire could then be derived using the Stefan-Boltzmann law with data from each image:

$$FRP = \sum_i \sigma \, a \, T_i^4 \tag{6}$$

where σ is the Stefan-Boltzmann constant (5.670374×10^{-8} Wm^{-2}K^{-1}), a is the pixel area (1.109×10^{-5} m^2), and T_i is the pixel brightness temperature (K). This sum was over the i pixels within each image that had T > 600 K, which excluded cooling non-combusting pixels (e.g., Freeborn et al., 2008; Wooster et al., 2011).

3.3.2 Fire effective temperature and FRP retrieval from spectral fits

Fire effective temperatures and FRP were also derived using UV-to-SWIR spectral radiance measurements collected at 0.14-0.25 Hz from a calibrated field spectrometer (SVC HR1024i; Table 1). Fire effective temperature estimates, akin to those coming from the Dozier (1981) 'dual-band' approach, were retrieved from the measured spectra (L$_{\lambda, \text{measured}}$) – though the use of hyperspectral data enabled three thermal components to be derived (similar to in Wooster et al., 2005; Dennison et al., 2006; and Amici et al., 2011). Modelled spectra (L$_{\lambda, \text{modelled}}$) that provided the best fits to the measured spectra were constructed from three individually modelled spectral radiances (L$_{FD}$, L$_{SD}$, and L$_C$) coming respectively from assumed flaming-dominated (FD, range 923-2000 K), smoldering-dominated (SD, 623-1023 K) and cooling (C, 280-623 K) emitters:

$$L_{\lambda, \text{modelled}} = \sum_i^{n=3} p_i \, B_\lambda(T_i) \tag{7}$$

where the fractional areas sum to 1, and $B_\lambda(T_I)$ the Planck radiance emitted by each fractional component was calculated using Eq. 4. Brightness temperature (T_i) and fractional area (p_i) of each component was iterated to provide the best match between L$_{\lambda, \text{modelled}}$ and (L$_{\lambda, \text{measured}}$).

A blackbody assumption was made during application of Eq. 7, and burns were conducted in the dark to prevent contamination by reflected sunlight. Due to the small distances involved in the measurement setup, no atmospheric

180 transmission adjustments were required to the spectra. CO_2 and H_2O absorption and emission regions could be seen in the measured spectra (e.g., at 1400, 1900 and 2500 nm in Fig. 2a) but were simply excluded from the model fitting process. Since little thermal emission occurs in the HR1024i spectral range from targets below ~500 K, the approach is not very well suited to retrieving temperatures below this limit. As per Wooster et al. (2005), FRP estimates were derived as the sum of the radiative emissions from the retrieved flaming and smoldering components:

$$FRP = A \sum_{i}^{n=2} \sigma \, p_i T_i^4 \tag{8}$$

185 where σ is the Stefan-Boltzmann constant A is the FOV area (0.064 m^2). This shall be referred to as the FRP retrieved using the spectral-fitting method, FRP$_{SF}$.

Figure 2 shows an example modelled and measured spectra from a single experimental burn, with excellent agreement seen outside of the previously mentioned gaseous absorption and emission regions.

FRP retrievals made using the thermal infrared brightness temperatures from the PI400 appeared to show good agreement

190 with those derived from the HR1024i VIS to SWIR spectra (see example in Fig. 3a). However, further validation investigations are required, such as in daytime retrievals. The data from the PI400 were subsequently used for all analysis since they provide a higher measurement frequency, and one that matches those of the AKBD measures (see Sect. 3.3.3). The PI400 data also provides spatially mapped FRP data rather than just a single 'fire-integrated' value.
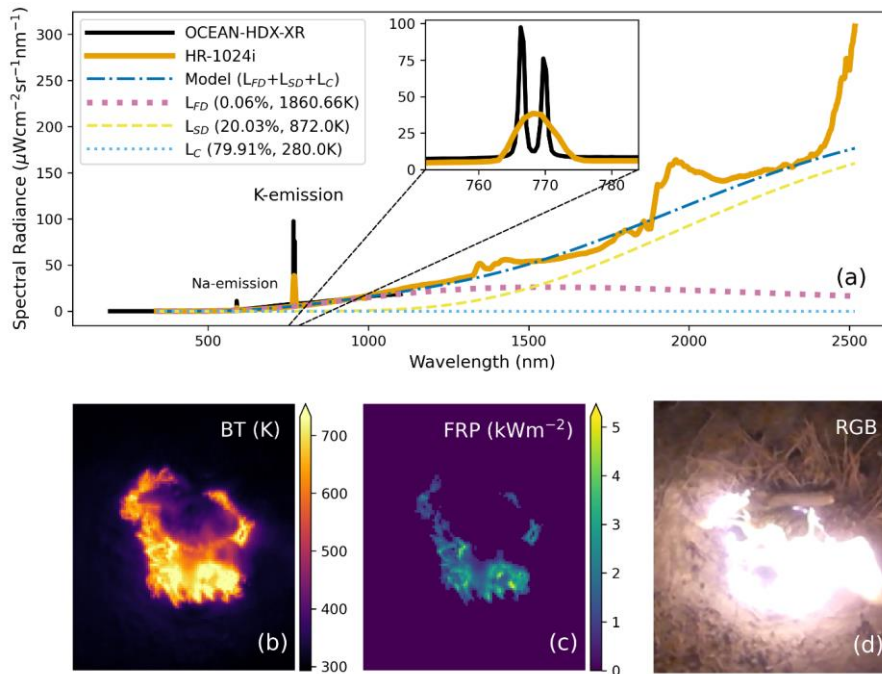
195

Figure 2. Snapshot of an exemplar 23 x 23 cm experimental pine forest litter fire viewed from nadir using the setup shown in Fig. 1. Fire is shown at the time of maximum flaming activity: (a) Fire radiative emission spectra as measured by the OCEAN-HDX-XR (Ocean Insight, UV-to-NIR) and HR1024i (SVC, UV-to-SWIR) spectrometers, with magnitudes adjusted for the FOV difference between the two instruments. Modelled spectra derived from the

200 **spectral-fitting method described in Sect. 3.3.2 and its three temperature components (retrieved fractional area (%) and temperature (K) are listed in the legend); (b) Temperature (K) measured by the PI400 (Optris); (c) Fire Radiative Power (FRP, kWm^{-2}) derived from the PI400 thermal imagery, as calculated via the Stefan-Boltzmann law and omitting pixels below 650 K (see Section 3.3.1); (d) Frame from RGB video camera.**
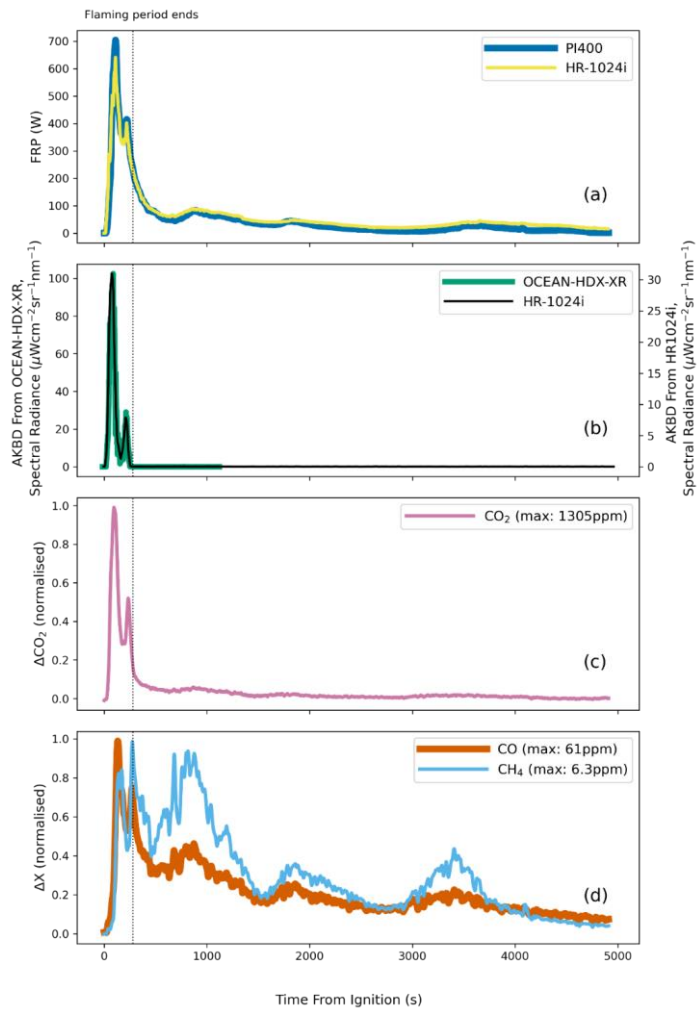
 Figure 3. Data from the exemplar pine forest litter fire shown in Fig. 2: (a) FRP time-series derived from brightness temperature imagery collected by the Optris PI400 thermal imager and VIS-to-SWIR spectral collected by the HR1024i. Data for a single time-step are shown in Fig. 2a; (b) Comparison of AKBD K-line metric derived from

spectra measured by the OCEAN-HDX-XR and HR1024i spectrometers around the location of the potassium emission line (see Sect. 3.3.3); (c) Time-series of excess (Δ) CO_2, CO and CH_4 (ppm) concentrations in the smoke from this fire, each normalized by their maximum value (given in the legend). The time flaming activity ceased as determined by the RGB video record is marked by the vertical dashed line.

3.3.3 K-line measurements

An OCEAN-HDX-XR spectrometer (Table 2) was used to provide 1 Hz K-line measurements of each fire. The instrument measurement diameter was 53 cm at the fuel bed, and the instrument calibrated to provide data in spectral radiance units using an Ocean Insight HL-3P-CAL calibration lamp. The resulting spectra were used to measure K-line strength using the AKBD metric introduced in Sect. 2.

The HR1024i can also provide K-line spectra, though its 3.5 nm spectral resolution in the K-line region is coarser than the 1.1 nm of the OCEAN-HDX-XR. Comparison of their AKBD data (e.g., Fig. 3b) showed excellent agreement (R^2 of 0.99; with a linear best fit of gradient of 0.381±0.002 and negligible intercept). However, the AKBD measured by the OCEAN-HDX-XR are more than twice as large as from the HR1024i. This is despite the former's larger measurement area; this is due to its higher spectral resolution, which is evident in its ability to better resolve the individual potassium emission lines (see Fig. 2a). Since the OCEAN-HDX-XR also provided a higher measurement frequency, its AKBD data were used for all subsequent analysis.

3.4 Smoke measurements

3.4.1 CO_2, CO and CH_4 mixing ratios

Trace gas measures of the smoke from every fire was continuously directed via the hood and through the extraction flue (Fig. 1), and used to calculate smoke emission rates and MCE. Continuous CO_2, CO and CH_4 mixing ratio measures were taken at an inlet at location C (Fig. 1) using an adapted Los Gatos Research (LGR) Ultraportable Greenhouse Gas Analyzer laser absorption spectrometer (described in Zhang et al., 2015). However, for the crop residue fires, the LGR was unavailable, so a GasLab CM-1000 was deployed instead. This instrument uses a Non-Dispersive Infrared (NDIR) detector to assess CO_2 mixing ratios, and an electrochemical sensor to assess CO. The differing response times of these two detectors

were accounted for using the method of Zhang et al. (2020) such that continuous MCE measurements could be derived using Eq. 1. Excess concentrations of CO_2, CO and CH_4, along with the matching FRP and AKBD data, are shown in Fig. 3c and 3d for an example pine forest litter fire.

235 ### 3.4.2 Trace gas emission rates

To account for any variability in the extraction system, the gas flow rates through the flue were calculated by combining the trace gas concentrations (Sect. 3.4.1), 1 Hz pressure difference measurements (dP [Pa]) between the inside and outside of the flue using a Testo 440, and the flue gas temperature using two thermocouples. Gas velocity (v [m s^{-2}]) was derived from the pressure data using the Bernoulli equation:

$$v = \sqrt{\frac{2dP}{\rho_X}} \qquad (9)$$

240 where ρ_X is the density of species X (kg m^{-3}). Temperatures of the flue gases varied by up to 40 K over the course of individual fires. Therefore, ρ_X was adjusted using:

$$\rho_X = \frac{MM_X P}{RT_{TC}} \qquad (10)$$

where MM_X is the molar mass of gas species X, R is the ideal gas constant (8.3145 $mol^{-1}K^{-1}$), P is pressure, which was assumed to be constant of 101 kPa as the pressure difference measurements from the Testo were negligible in comparison, and T_{TC} is the temperature recorded by a thermocouple in the flue (in K). The measured emission rate of X, $\left(\frac{dM_X}{dt}\right)_m$, in g s^{-1}

245 was then calculated by:

$$\left(\frac{dM_X}{dt}\right)_m = A_{CS}\rho_X v 10^{-6}\Delta X \qquad (11)$$

where A_{CS} is the cross-sectional area of the flue at location D (0.01767 m^2) and ΔX is the excess concentration of X (in ppm) in the flue and 10^{-6} is a unit conversion factor for the gas concentration.

3.4.3 Experimental Procedure

In total, 12 pine forest litter, 12 oak kindling, and 8 crop residue fires were conducted over a period of 1 week, during which

250 ambient air temperature in the Chamber ranged from 9 to 12°C and relative humidity from 71 to 75%. After preparation of

each fuel bed, the extraction flue and all instruments were turned on and the pre-fire trace-gas ambient concentrations calculated as the mean of the sixty 1 Hz concentration measurements taken immediately before each ignition. Ignition was made using a blowtorch applied to one edge of the fuel bed, with a small amount of sawdust added to help ignite the oak kindling. Measurements only ceased when concentrations of CO_2 and CO closely approached those pre-fire. Post-fire, the cooling char, ash, and any unburned fuel was removed and the next fuel bed prepared. Fuel mass ranged from 125 g to 250 g for the pine litter fires, 220 g to 410 g for oak, and 100 g to 200 g for crop residue. Fire duration across the 32 burns ranged from 16 to 42 minutes.

4. Laboratory experiment results

4.1 K-line detection

As with previous work (Amici et al., 2011; Magidimisha and Griffith, 2017; Vodacek et al., 2002), the detection of a K-line signature coincided with clear flaming combustion seen in the RGB video record. An AKBD $\geq$ 1.5 $\mu Wcm^{-2}sr^{-1}nm^{-1}$ was always recorded by the OCEAN-HDX-XR when flames were visible. A higher MCE was also recorded when the AKBD signal was high, indicating that a higher proportion of fuel carbon was being completely oxidized to CO_2 than when the AKBD was low. We built on these observations to attempt to link the K-line emission signal to quantitative improvements in our ability to estimate the trace gas emission.

4.2 Fire effective temperature and spectral fitting

Figure 4 shows the fire effective temperature and area parameters derived using fits to the spectra of a single pine forest litter fire. Whilst the total FRP from these fits agrees with that derived using the PI400 as already stated (Fig. 3a), the individual FRP calculated for the separate flaming and smoldering components do not appear very realistic. The highest combustion rate is seen in the period from ignition to when all flaming activity ceased, and it is here that the highest rates of CO_2 production occur (Fig. 3c). However, the 'flaming FRP' is reported as far smaller than the 'smoldering FRP' even during this period (Fig. 4a), even though fuel consumption was clearly dominated by flaming combustion at this time (also shown by the CO_2 production in Fig. 3c). Therefore, these separate flaming and smoldering FRP components do not appear well matched to how each combustion phase is actually contributing to overall fuel consumption.
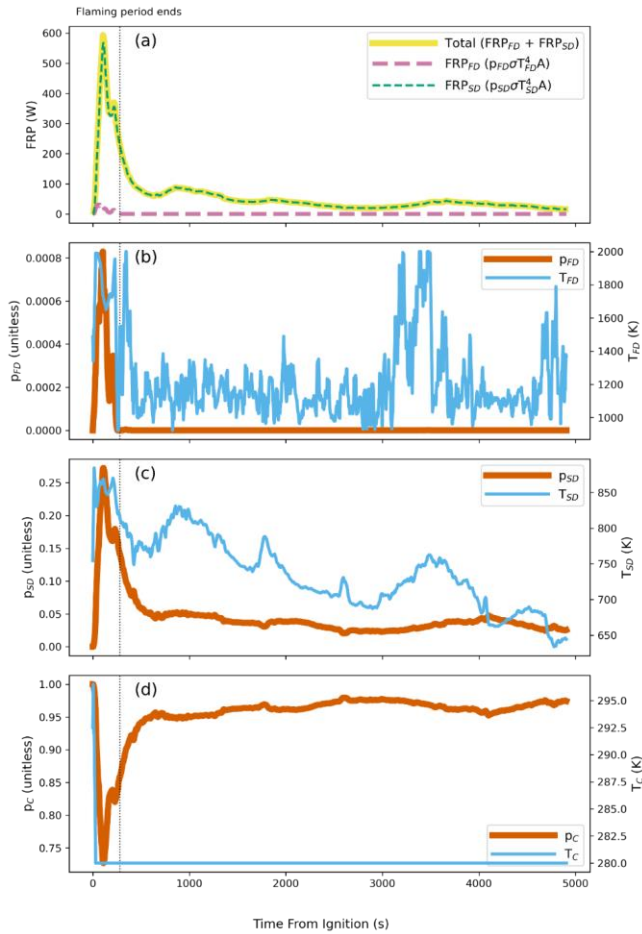
275

Figure 4. Time-series of results of the spectral-fitting method for the pine forest litter fire also shown in Fig. 3: (a) FRP derived from the two separate fire components (Eq. 6), the first is meant to represent the flaming zone (923 K < T_{FD} < 2000 K), the second the smoldering zone (623 K < T_{SD} < 1023 K), and their sum is the total of these two; (b) The fractional area, p_{FD}, and temperature, T_{FD}, of the first component representing flaming-dominated combustion; (c)

280 **The fractional area, p_{SD}, and temperature, T_{SD}, of the second component representing smoldering-dominated**

combustion; (d) The fractional area, p_C, and temperature, T_C, of the third component representing the cooling non-fire background. The end of the flaming period, the time when all flames appeared to cease in the RGB camera data, is indicated by the vertical dotted line.

285 Going further, for all fires on which this method was tested, we found that retrievals of the second fire component derived from the spectral fits and meant to represent the smoldering combustion contribution always dominated the total FRP. In contrast, retrieved temperatures in the flaming zone (T_{FD}) were frequently very high, often above 1600 K during the flaming period of Fig. 4b for example, but those of p_{FD} (flaming proportional area) very small (e.g., never larger than 0.085%) – which led to a low contribution to total FRP. As there is little emission from the cooler smoldering component in the spectral

290 region measured, this 'flaming' component is derived by fitting at shorter wavelengths and some of this signal is coming from hot soot in the flames rather than from the burning fuel itself. Parameters such as flame depth and soot concentration, which are significant drivers of flame emissivity (Johnston et al., 2014), therefore influence the retrievals. Similar to the AKBD measurements, we observed that flames were present while $f_1 \geq 0.0016\%$ (Fig. 4a). However, any daytime measurements will require the removal of the reflected solar radiation component present at VIS to SWIR wavelengths

295 (discussed further in Sect. 5.1.2). This task that can introduce large uncertainty, especially when dealing with course spatial resolution imagery where at the shorter wavelengths the solar reflected signal maybe far larger than that from the fire. The AKBD calculation is unaffected by this issue since it quantifies the strength of the K-line above the combination of reflected solar radiation and Planckian emission signal.

4.3 Combustion phase emission relationships

300 Figures 5a, 5b and 5c show, respectively, how emission rates of CO_2, CO and CH_4 vary with FRP – in this case for the example pine forest litter fire. Each data point is colored by MCE, indicating the mix of smoldering, and flaming combustion ongoing at each measurement time. High MCE (maximally dominated by flaming combustion) is yellow, and lower MCE (maximally dominated by smoldering combustion) is in dark blue. Points having a contemporaneous AKBD signal ≥ 1.5 $\mu Wcm^{-2}sr^{-1}nm^{-1}$ are outlined, indicating the confirmed presence of flaming combustion via the K-line signal.

305 It is clear from the hysteresis-shaped patterns present in Fig. 5 that any assumption of a purely linear relationship between trace gas emission rate and FRP is flawed, and that instead such relationships are combustion phase dependent. This agrees with previous lab-based studies comparing FRP to CO_2 and CO emission rates (e.g., Freeborn et al., 2008).

Generally, soon after ignition, the fires enter a 'flaming-dominated' stage that produces a steep linear increase in CO_2 production with increasing FRP (Fig. 5a). Smoldering can and does occur during this 'flaming-dominated' stage, but it is

310 consuming very little of the fuel compared to flaming. This is different to the 'flaming period' – which we class as the period of the burn when flames are present as defined via AKBD thresholding. During this time, significant smoldering combustion can also occur, particularly as the fire is transitioning away from the flaming-dominated stage. As the smoldering-dominated stage begins (no flaming activity), there also appears to be a linear relationship between FRP and CO_2 emission, but with a gradient far lower than that found during the flaming-dominated stage. During the flaming period, the data of Fig. 5a falls

315 between the two linear clusters representing the flaming-dominated and smoldering-dominated stages, with MCE values indicating a mixed contribution from both flaming and smoldering activity.

As expected, for the 'preferentially smoldering' species CO (Fig. 5b) and CH_4 (Fig. 5c), the relationship between FRP and trace gas emission rates are opposite in nature to those of the 'preferentially-flaming' CO_2 (Fig. 5a). The emission rates of CO and CH_4 increase linearly with FRP, but with a slope significantly lower than that for CO_2 during the early flaming-

320 dominated stage. During the smoldering-dominated stage however, these slopes increase but the data are less well fitted by a linear relationship than during the flaming-dominated stage. The latter is possibly contributed to by a lower plume buoyancy during the smoldering-dominated stage, when some of the smoke may not have made it directly into the extraction flue.

Based on these data, we developed and tested three different empirical models that use the remotely sensed measures to estimate the fires trace gas emission rates. The first model uses only remotely sensed FRP measures - and supposes a 'fire-

325 averaged' relationship between FRP and trace gas emission rate, which is assumed for example within the classical Fire Radiative Energy Emissions (FREM) approach developed for use with satellite FRP data (Mota and Wooster, 2018; Nguyen et al., 2023; Nguyen and Wooster, 2020). The second two models use the K-line measures in addition to FRP and are aimed at providing a more nuanced trace gas emission rate estimate by considering the different relations seen during flaming and smoldering combustion. We used data from 23 'training' fires across all fuel types to develop the parameters of each model.

330   Nine were randomly selected from each of the pine forest litter and oak kindling burns, and five from the crop residue burns.

Three fires of each fuel type were then used to evaluate, or 'test', the models.
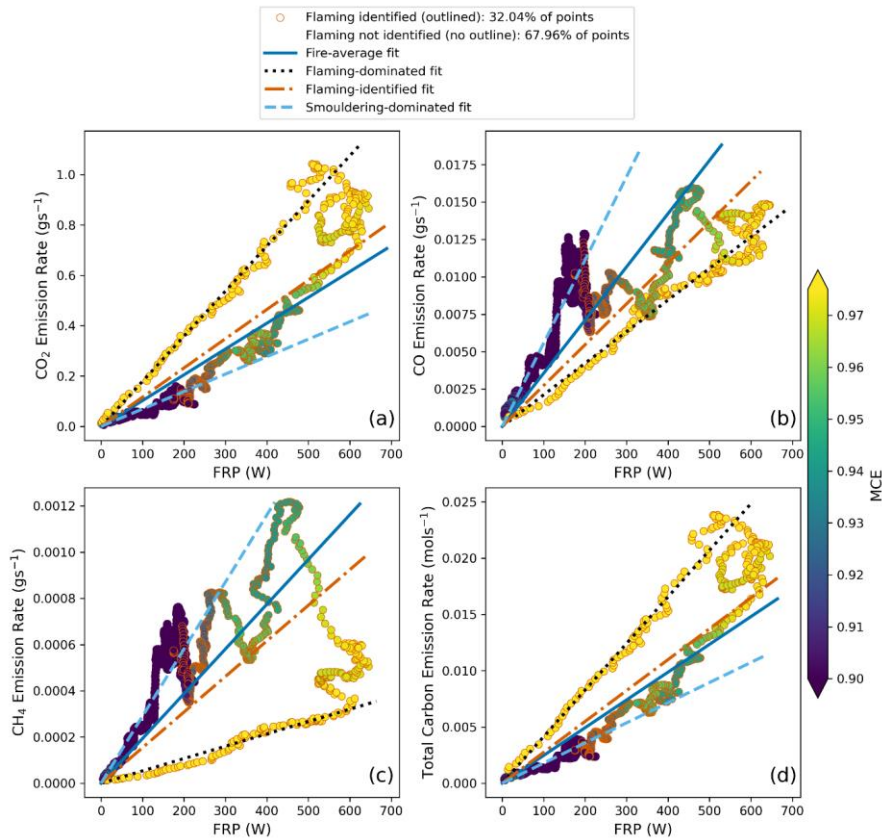
Figure 5. Relationships between trace gas emission rate and FRP for (a) CO_2, (b) CO, (c) CH_4, and (d) total carbon flux in moles (i.e., moles of CO_2, CO and CH_4). FRP here is derived from the PI400 brightness temperature imagery

335   **as described in Section 3.3.1. These data are from a single pine forest litter training fire (Fire 11), and each point is colored by its MCE at the time of measurement, and those when AKBD > 1.5 $\mu Wcm^{-2}sr^{-1}nm^{-1}$ (as derived from the OCEAN-HDX-XR) indicating the presence of some flaming activity (flaming period) are distinguished from**

smoldering-dominated points by their outline. Emissions coefficients for flaming-dominated (MCE > 0.975), flaming-identified (AKBD ≥ 1.5 µWcm^{-2}sr^{-1}nm^{-1}), fire-average and smoldering-dominated (AKBD < 1.5 µWcm^{-2}sr^{-1}nm^{-1}), which were calculated from the 'training' fires (including Fire 11) and are presented in Table 2.

4.4 Emission models account for combustion phase

4.4.1 Model 1: fire-average

As with the FREM approach this model assumes a simple linear relationship between FRP and trace gas emission rate of species X, $\left(\frac{dM_X}{dt}\right)_{modelled}$.

$$\left(\frac{dM_X}{dt}\right)_{modelled} = C_A^X FRP \qquad (12)$$

where the average emission coefficient C_A^X, was calculated by dividing the sum of all emission rate measures by the sum of all FRP measures. This model acts as a baseline to which the performance of the further two models that incorporate K-line information could be compared. C_A^X values for the three fuels are presented in Table 2.

Table 2: Emission coefficients, C_{CPh}^X, for the trace gas emission rates of CO_2 and CO (and CH_4 where measured), for each combustion phase (CPh) scenario (fire-average, flaming-dominated, flaming-identified, smoldering-dominated) for pine forest litter, oak kindling and crop residue fires. Units are g s^{-1} MW^{-1}.

Trace Gas Emission Coefficients (g s^{-1} MW^{-1})					
		Fire-average (A)	Flaming-dominated (FD)	Flaming-identified (FI)	Smoldering-dominated (SD)
Pine forest litter	CO_2	880 ± 2	1560 ± 12	1100 ± 4	523 ±2
	CO	33.4 ± 0.1	15.0 ± 0.1	25.8 ± 0.1	45.5 ± 0.1
	CH_4	2.03 ± 0.01	0.586 ± 0.008	1.53 ± 0.005	2.82 ± 0.01
Oak kindling	CO_2	888 ± 2	1950 ± 44	1030 ± 3	464 ± 2
	CO	22.8 ± 0.1	3.58 ± 0.08	18.0 ± 0.1	37.0 ± 0.1

	CH$_4$	0.792 ± 0.002	0.0741 ± 0.002	0.749 ± 0.002	0.922 ± 0.003
Crop residue	CO$_2$	804 ± 6	1670 ± 40	982 ± 10	434 ± 5
	CO	42.4 ± 0.4	16.4 ± 1.1	43.3 ± 0.6	40.5 ± 0.8

4.4.2 Model 2: FRP and AKBD magnitude (FAM)

In this second model, the emission rate of trace gas species X was modelled as the sum of that coming from separately considered flaming and smoldering activity:

$$\left(\frac{dM_X}{dt}\right)_{modelled} = C_{FD}^X FRP_{FD} + C_{SD}^X FRP_{SD} \tag{13}$$

where FRP_{FD} and FRP_{SD} are the contributions of the flaming-dominated (FD) and smoldering-dominated (SD) components of the fire to total FRP (i.e., $FRP_{FD} + FRP_{SD} = FRP$). C_{FD}^X and C_{SD}^X are the flaming-dominated and smoldering-dominated emission coefficients between FRP and the emission rate of species X. Values for C_{FD}^X were derived by ratioing the total amount of species X emitted by the total FRP released for data during the time when MCE exceeded a threshold that produced the highest R^2 for a linear fit (e.g., MCE > 0.975 for pine). For the smoldering emission coefficients (C_{SD}^X) only data when AKBD < 1.5 µWcm^{-2}sr^{-1}nm^{-1} were used since this confirmed the absence of flaming combustion. Examples are shown in Fig. 5, with the derived emissions coefficients for each fuel shown in Table 2.

This model requires distinguishing the relative contribution of each combustion phase to the total FRP recorded at any particular time. By assuming that FRP_{FD} is directly proportional to AKBD (i.e. $FRP_{FD} = m_k$ AKBD, where m_k is a constant) Eq. 13 becomes:

$$\left(\frac{dM_X}{dt}\right)_{modelled} = C_{FD}^X\left(m_k^{\square}\ AKBD\right) + C_{SD}^X\left(FRP - m_k^{\square}\ AKBD\right) \tag{14}$$

where AKBD > 1.5 µWcm^{-2}sr^{-1}nm^{-1} to exclude noise. m_k values were determined by solving Eq. 14 with the measured AKBD, FRP and emission rates of the training fires using a least-squares approach. Mean and standard errors for the three fuels were: 4.99±0.04 W(µWcm^{-2}sr^{-1}nm^{-1})$^{-1}$ (pine), 5.90±0.32 W(µWcm^{-2}sr^{-1}nm^{-1})$^{-1}$ (oak) and 3.25±0.79 W(µWcm^{-2}sr^{-1}nm^{-1})$^{-1}$ (crop residue). Although these standard errors do not overlap, the values of m_k are rather close to one another, and this was unexpected given that different fuels are likely to contain different concentrations of potassium. However, use of a

370 single fuel-independent m_k is very useful as it means any future application of the method would not need to know the fuel

type that is burning. Therefore, we selected the mean m_k, along with its propagated uncertainty, of 4.71 ± 0.28 $W(\mu Wcm^{-2}sr^{-1}nm^{-1})^{-1}$ for use with all fuels to in the performance assessment stage, which was based on the nine test fires. Since this model

relies on quantifying the strength of the potassium emission signal, we refer to it herein as the FRP and AKBD Magnitude

(FAM) method or Model 2.

4.4.3 Model 3: FRP and AKBD identification (FAI)

As with the FAM model, this third model also considers the K-emission and FRP of the fire, but only uses the K-line

presence or absence, rather than its magnitude. The rational for this is that NIR wavelength radiation maybe significantly

scattered by smoke in thick wildfire plumes, perhaps altering the measured AKBD magnitude. The model therefore does not

attempt to separate FRP_{FD} and FRP_{SD}, but instead multiplies the total FRP by different emission coefficients depending on

380 whether or not a K-line is detected:

$$\left(\frac{dM_X}{dt}\right)_{modelled} = C_{FI}^X FRP, \text{ when AKBD} \geq 1.5 \ \mu Wcm^{-2}sr^{-1}nm^{-1} \tag{15}$$

$$= C_{SD}^X FRP, \text{ when AKBD} < 1.5 \ \mu Wcm^{-2}sr^{-1}nm^{-1} \tag{16}$$

where C_{SD}^X is the same smoldering-dominated FRP-emission rate gradient from the FAM method in Eq. 13 for when no

flaming is identified. Then, for when some flaming combustion is detected, FRP is instead multiplied by a 'flaming-

identified' ratio, C_{FI}^X. This was calculated by dividing the total emission of X by the total FRP when AKBD > 1.5 $\mu Wcm^{-2}sr^{-1}nm^{-1}$, i.e. during the flaming periods of the training fires. Examples for the three trace gases are shown in Fig. 5. The

385 average across all fires for every fuel type tested are presented in Table 2.

4.5 Emission model evaluation and intercomparison

The performance of the three different remote sensing-based models in estimating trace gas emission rates were evaluated,

with results for one of the pine forest litter fires shown in Fig. 6. Figure 6a shows the FRP time series, and Fig. 6b the

AKBD time series. Using combinations of these data, the conventional, fire-average Model 1 underestimates CO_2 production

390 compared to reality during the early stages of a fire when flaming activity dominates, and then overestimates it during the

subsequent smoldering stage. This can be seen in Fig. 6c, for example, and is a consequence of the relationship found

between FRP and CO_2 emission rate described in Sect. 4.3 and Fig. 5a. Likewise, the results for CO and CH_4 production act in the opposite direction to those of CO_2, these being generally overestimated during the flaming-dominated stage and underestimated during the smoldering stage (see Supplementary Materials).

In addition to the total measured FRP, Fig. 6a also presents the estimated contribution of flaming and smoldering combustion to the FRP signal – based on the FAM (Model 2) approach. The FRP is initially totally dominated by flaming combustion, but variable amounts of smoldering combustion then commence and eventually become dominant. This pattern appears much more realistic than the flaming and smoldering contributions to FRP calculated using the spectral-fitting approach (Sect. 4.2), which significantly underestimates flaming phase contributions to overall FRP. Model 2 also produces an estimated trace gas emission rate time series that is in far better agreement with the trace gas measures than are those from the fire-average Model 1. The comparison in Fig. 6d indicates that RMSE for the FAM model is less than half that of the fire-average approach, and the average RMSE reduction is reported in Table 3. For CO_2 these reductions were very significant; 58±4% (pine); 46±4% (oak) and 35±13% (crop residue). For CO and CH_4 they are less significant, and the FAM (Model 2) approach showed little ability to improve upon the ability to estimate CO emission rates of the oak fires compared to Model 1 (-1.2±14.4 %). While the FAM approach produced a smaller instantaneous error for estimating CO than the fire-average approach for two of the three test fires, for the third the estimate was much poorer (see Fig. A6), which affected the average performance. However, there was some improvement for the other two fuel types, and in general Model 2 improves CO and CH_4 emission rate estimation compared to Model 1 - but to a far lesser extent than for CO_2. However, for MCE the improvements provided by Model 2 over Model 1 are very significant, even for the oak fires. The reduction in RMSE compared to the fire-average approach ranges from 40±7% (soy) to 54±6% (pine).

Like the FAM approach, the FAI method (Model 3) also uses AKBD measures - but now just in a binary 'on/off' fashion, as detailed in Sect. 4.4.3. The approach proves significantly more accurate in terms of trace gas emission rate estimation than does the 'fire-average' approach (Model 1) but does not perform as well as the FAM approach. For example, the reduction in RMSE for instantaneous MCE estimations is lower, ranging from 17±6% (soy) to 37±12% (pine).

Overall, our results from these combustion chamber burns indicate that FRP-based estimates of trace gas release rates can be greatly improved via the addition of K-line measurements. We also tested modified versions of the Model 2 (FAM) and 3

(FAI) approaches that estimated fuel combustion rate prior to trace gas emissions, but the performance was almost identical to that without this additional step (see Appendix B). This work indicates that the relationship between FRP and combustion rate differs significantly between smoldering and flaming combustion.
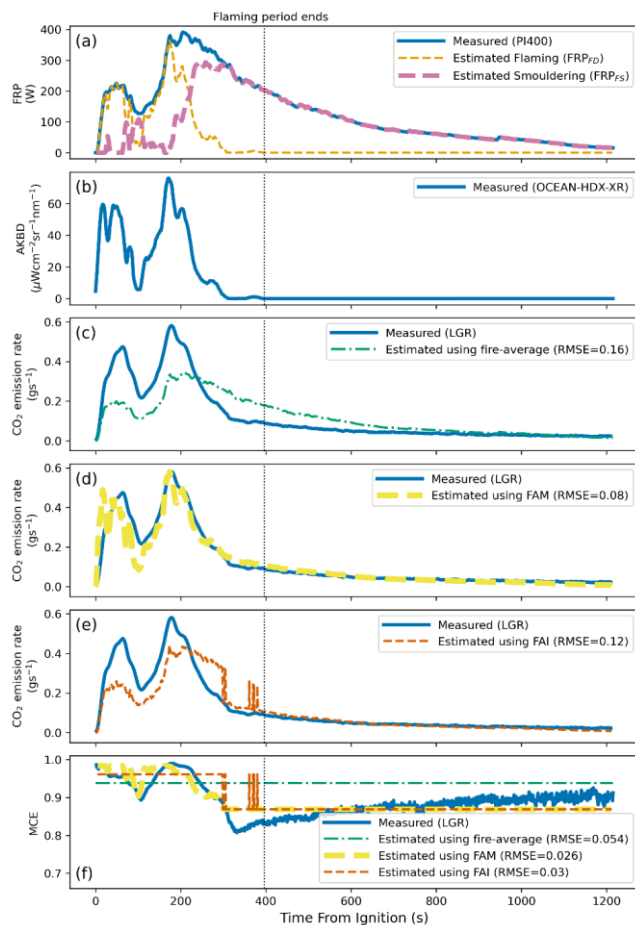
Figure 6. FRP, AKBD and trace gas emission rate time series for an exemplar pine forest litter 'test' fire (Fire 3). (a) FRP (W) calculated from the PI400 thermal imagery, along with the estimated flaming and smoldering components

derived from this and the complementary AKBD measures; (b) AKBD ($\mu Wcm^{-2}sr^{-1}nm^{-1}$) derived from spectra recorded by the OCEAN-HDX-XR spectrometer; trace gas emission rate of CO_2 (gs^{-1}) compared to that estimated with (c) the fire-average approach (Model 1); (d) the FAM approach (Model 2); (e) the FAI approach (Model 3); and (f) measured and modelled MCE. The end of the flaming period as determined by the RGB video camera record is denoted by the vertical dotted line.

Table 3: Mean RMSE between the measured and three modelled emission rates and MCE for each fuel type. Also includes the mean difference in RMSE for the FAM (Model 2) and FAI (Model 3) approaches compared to the fire-average (Model 1) method (%).

		Approach Used to Estimate Emissions				
Fuel	Trace Gas Species and MCE	Model 1: fire-average	Model 2: FAM		Model 3: FAI	
		Mean RMSE	Mean RMSE	Mean difference with fire-average (%)	Mean RMSE	Mean difference with fire-average (%)
Pine forest litter	CO_2 (gs^{-1})	0.18±0.02	0.10±0.02	**-46±7**	0.13±0.02	**-27±3**
	CO (mgs^{-1})	3.9±0.3	3.5±0.5	**-12±6**	3.7±0.6	**-6.1±9.2**
	CH_4 (mgs^{-1})	0.49±0.04	0.37±0.04	**-26±2**	0.44±0.02	**-9.6±5.6**
	MCE	0.048±0.003	0.022±0.002	**-54±6**	0.029±0.004	**-37±12**
Oak kindling	CO_2 (gs^{-1})	0.45±0.14	0.24±0.08	**-46±4**	0.40±0.13	**-14±3**
	CO (mgs^{-1})	6.1±0.5	6.1±1.1	**-1.2±14.4**	5.7±0.9	**-8.8±7.5**
	CH_4 (mgs^{-1})	0.43±0.04	0.41±0.03	**-4.9±1.3**	0.43±0.06	**-2.6±4.6**

	MCE	0.056±0.003	0.032±0.001	**-43±3**	0.035±0.005	**-37±7**
Crop residue	CO_2 (gs^{-1})	0.32±0.03	0.19±0.03	**-35±13**	0.28±0.02	**-10±1**
	CO (mgs^{-1})	8.0±1.3	5.7±0.3	**-23±12**	7.0±0.6	**-7.7±8.5**
	MCE	0.052±0.007	0.030±0.001	**-40±7**	0.042±0.002	**-17±6**
Average across all fuels	CO_2			**-42±15**		**-17±4**
	CO			**-12±20**		**-7.5±14.6**
	CH_4			**-15±5**		**-6.1±7.2**
	MCE			**-46±10**		**-30±15**

5. Applications to airborne data

5.1 Methodology

5.1.1 Airborne data

The results in Sect. 4 show the benefits of combining remotely sensed FRP and AKBD measures when estimating trace gas emission rates of small-scale laboratory fires. However, ultimately, we aim at applications based on satellite EO measures and real landscape burning. Whilst satellite-derived K-line measurements from space have only been demonstrated once (Amici et al., 2012), the increasing launch of spaceborne imaging spectrometers provides the possibility for more routine observations with the necessary spatial/spectral resolution. Whilst we wait for those data, we here demonstrated the approach using airborne EO of real wildfires burning in the boreal forests of northern Ontario, Canada. The airborne remote data used comes from the Specim FENIX VIS-to-SWIR hyperspectral imager, covering the same spectral range with the same FWHM spectral resolution in the K-line region as the HR1024i, meaning we could apply essentially the same approaches and models developed in our laboratory study (Sect. 3.3.2 and 3.3.3).

5.1.2 FRP and K-line retrievals

Our FRP retrieval process required slight modification for the airborne EO application, in order to account for the reflected solar radiation present in the daytime imagery. For this, areas of water were masked from the scene and the active fire pixels detected using the HFDI index (Dennison and Roberts, 2009). All 'non-fire' pixels were then categorized into 'burned' and 'unburned' using the classification process of Waigl et al. (2019). Mean 'burned' and 'unburned' spectra were calculated using 200 pixels of each class, and these incorporated into the spectral-fitting model (Eq. 6) applied to each active fire pixel:

$$L_{\lambda,\ measured} = p_u L_{\lambda,\ u} + p_b L_{\lambda,\ b} + \sum_{i}^{n=3} \varepsilon\ \tau\ p_i\ B_\lambda(T_i) \qquad (17)$$

where $L_{\lambda,\ u}$ and $L_{\lambda,\ b}$ are the mean radiance calculated in the neighboring unburned and burned pixels at wavelength λ and p_u and p_b are their area fractions of the pixel. All fractional areas sum to 1. The final component is the same as that used previously.

For inclusion in Eq. 17, the MODTRAN atmospheric radiative transfer model (Berk et al., 1999) was used to estimate atmospheric transmittance (τ) from the surface to the aircraft altitude of 2500 m, assuming a 1976 US standard atmosphere, a 23 km visibility and an atmospheric CO_2 concentration of 420 ppm. As with the laboratory data, only wavelengths above 1200 nm were included in the spectral fitting approach and application of Eq. 16 to each active fire pixel, in order to reduce the influence of atmospheric scattering by smoke. Per-pixel FRP was again calculated from the derived p_i and T_i values using the Stefan-Boltzmann law (Eq. 7). Figure 7c shows measured and modelled spectra of a single example active fire pixel, and as with the HR1024i data (Fig. 2a) the two agree extremely well.

As this FRP retrieval method relies mostly on the second, smoldering temperature component (L_{SD}), it is likely to still be valid despite the unknown influence of reflected solar radiation at the smaller wavelengths on L_{FD}. Although further validation efforts are required to confirm this. On the other hand, relying on a non-zero value for the fractional area of L_{FD} to indicate flaming combustion is no longer valid. The retrieved p_{FD} for many pixels was often zero, whilst the magnitude of the AKBD parameter indicated flaming combustion was present. The opposite was also true: many pixels with a significant p_{FD} had a very low or zero AKBD. Therefore, AKBD was more trusted than p_{FD} for indicating the presence of flaming combustion since the measurement was not influenced by reflected sunlight.
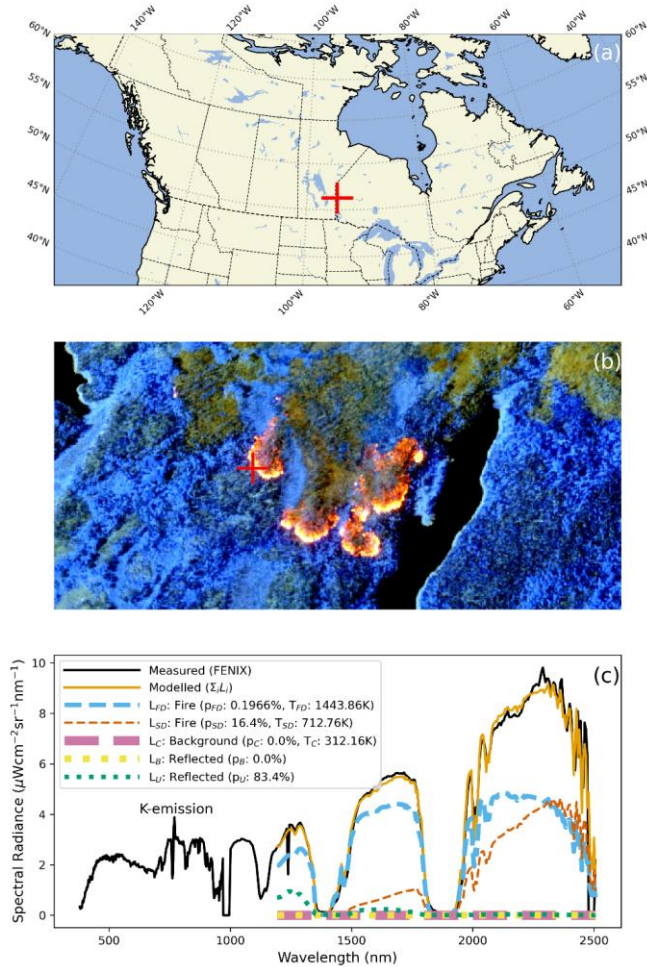
Figure 7. Daytime airborne VIS-SWIR data taken on 11th August 2018 using a Specim FENIX hyperspectral imager flown over a boreal forest wildfire burning in Northwestern Ontario, Canada: (a) Map showing fire location (51.293° N, 94.805° W); (b) Infrared color composite image comprised of data collected in bands centered at 2.2, 1.6 and 1.1 microns (RGB) with spatial resolution of 4m, the scene is 1020 m x 2160 m; (c) Exemplar spectra (VIS to

SWIR) of an active fire pixel (location shown in the infrared color composite (b)), with the best matched modelled spectra derived using the spectral-fitting approach (Eq. 16), along with the individual components that sum to that spectra: L_{FD} (fire, flaming-dominated), L_{SD} (fire, smoldering-dominated), L_b (background/cooling fuel), and the reflected sunlight components L_U (unburned) and L_B (burned).

The emission coefficients for the pine forest litter fuel, shown in Table 2, were used to convert the derived per-pixel FRP values to trace gas emission rates. For the FAM approach, the proportionality constant (m_k) linking AKBD and flaming FRP (Eq. 13) was taken from the mean of 0.0201 ± 0.0012 W(μWcm^{-2}sr^{-1}nm^{-1})$^{-1}$ determined for the three different fuels, with this value including an adjustment for differences between the pixel size and FWHM of the FENIX and HR1024i instruments. The same value was used in all results presented in Section 4 (and the Appendix).

5.2 Airborne data results

Figure 8a shows a true color composite of the wildfire, complementing the infrared color composite shown in Fig. 7. Thick smoke blows away from the fire front, masking much of the land and supporting the decision to base FRP retrieval on wavelengths longer than 1200 nm less affected by Mie scattering (Sect. 5.1.2). By contrast, the longer NIR and SWIR wavelengths are far less affected, and the land and fire can be viewed clearly through the smoke (Fig. 8a). Figure 7b maps the FRP of each active fire pixel based on the spectral fitting method (see the example at a single pixel shown in Fig. 8b). Non-fire pixels are here colored depending on their proportion burned – p_B and p_U (Eq. 17). Overall, the imagery shows five fire front heads having high-FRP and likely flaming activity advancing against the wind, with lower FRP areas in the (presumed largely smoldering) zone behind.

Figure 8c maps AKBD, used to class fire pixels as flaming or smoldering. The AKBD map indicates that flaming activity is indeed present in the high FRP fire front pixels, and only a few lower FRP spots of flaming activity exist in the largely smoldering zone. Applying the FAM approach, Fig. 8e, 8f and 8g show estimated CO_2, CO and CH_4 emission rates for the fire, and Fig. 8h the MCE. Higher MCE smoke is emanating from the flaming fronts, and lower MCE from the smoldering zone apart from the few spots still flaming.
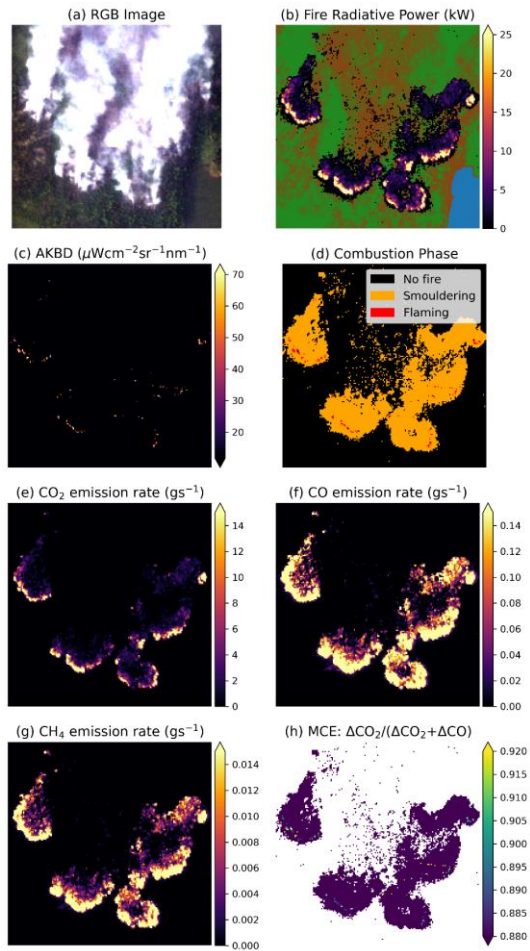
Figure 8. 4 m spatial resolution airborne imagery and derived fire and smoke characteristics of the wildfire shown in Fig. 7. This scene is 700 m x 700 m wide. (a) RGB color composite to compare to the SWIR color composite shown in Fig. 7b; (b) FRP derived using spectral-fitting approach (Eq. 16), with non-fire pixels colored depending on whether they are classed as burned (brown) and unburned (green) via the method discussed in Sect. 5.1.2 , masked out water

pixels of a lake in the bottom right of the scene are shown in blue; (c) AKBD derived using Eq. 5 (Sect. 2); (d) Combustion phase of each active fire pixel derived from an AKBD threshold of 0.57 µWcm^{-2}sr^{-1}nm^{-1}; emission rate derived using the FAM approach of (e) CO$_2$; (f) CO and (g) CH$_4$; along with (h) the MCE estimated using the same approach.

505   The total emission rate of CO$_2$ for the entire fire is estimated using the FRP and AKBD data by the FAM (Model 2) as 20.2±0.1 kgs^{-1}, with a relatively similar 22.9±0.2 kgs^{-1} estimated from Model 2 (FAI). Each is significantly lower than the 33.5±0.2 kgs^{-1} estimated using the Model 1 (FRP only) approach with the 'fire-averaged' emissions coefficient, essentially because this approach overestimates CO$_2$ emission rate when smoldering combustion is dominant (see Fig. 5a and 6c). The degree of overestimation could have been worse because only 1.4% of the detected active fire pixels in the airborne image of

510   Fig. 8 contain flaming activity.

Since the majority of the fuel consumption is coming from smoldering combustion, the FAM and FAI approaches estimate higher emission rates for CO and CH$_4$ than does the fire-average approach. For CO the models estimate the following: 1270±10 gs^{-1} (fire-average), 1720±10 gs^{-1} (FAM) and 1630±10 gs^{-1} (FAI), and for CH$_4$: 77.2±0.6 gs^{-1} (fire-average), 107±1 gs^{-1} (FAM), and 100±1 gs^{-1} (FAI). Therefore, whilst flaming combustion contributes around 2.4% of total CO$_2$ production, it

515   contributes only around 0.3% and 0.2% of CO and CH$_4$ production, respectively. Flaming combustion is therefore responsible for around 2% of the fuel consumption rate.

Since the wildfire smoke contained copious amounts of particulates (Fig. 8a), altered (and even missed) AKBD measurements may have resulted from Mie scattering. Therefore, this may make the FAI approach more appropriate than the FAM approach. Overall, while the trace gas emission rate estimates from the FAM and FAI approaches are relatively similar

520   (535±6 and 592±9 mols^{-1} of carbon), they are very different to those of the fire-average approach (811±10 mols^{-1} of carbon). Their application accounts for the fact that the fire is mostly smoldering – information that would otherwise be missed.

6. Summary and conclusions

Combustion phase and the proportion of flaming and smoldering activity occurring in landscape fires varies with fuel type and fuel characteristics. This, in turn, influences the rate of fuel consumption and smoke emission, along with the smoke

525 emissions chemical composition via its effect on the emissions factors (EFs) of the individual emitted chemical species. There is increasing interest in tailoring the EFs applied within fire emissions estimates, for example to cope with the presumed seasonal variations in emissions factors (Vernooij et al., 2023, 2022). Earth observation has long been suggested as a way to do this, by remotely mapping combustion phase to improve global smoke emissions estimation. We have provided the first attempt at evaluating whether such methods actually lead to the desired improvements, using laboratory

530 burns of three fuel types to test two approaches of determining combustion phase that (i) use remotely sensed retrievals of sub-pixel fire temperature, and (ii) utilization of potassium emission line (K-line) signatures that only occur during flaming combustion.

Whilst the first approach produced fire temperature estimates that were able to provide accurate FRP values, the individual fit parameters were not easily related to the smoke emissions characteristics. On the other hand, measurements of the K-line

535 emission strength were related to the emission rates of CO_2, CO and CH_4, leading us to develop two empirical models that used (Model 2) the magnitude of the K-line emission strength, and (Model 3) only its identification and combined these with the FRP data to better estimate fire smoke emissions rate and smoke chemical composition.

When compared to the standard FRP-only approach (Model 1) used to represent classical smoke emission estimate methods, the combination of FRP and K-line data significantly increased the accuracy of the resulting emission rate estimates of the

540 trace gases examined. It also significantly improved estimation of the modified combustion efficiency (MCE) of the fires smoke plumes, which directly relates to the contribution of flaming and smoldering combustion to the smoke. We did not find the ability to remotely determine sub-pixel fire effective temperature to provide similar improvements.

The FRP and K-line magnitude approach (Model 2) reduced the RMSE of the MCE estimates for the emitted smoke by between 54±6% and 40±7%, depending on fuel type, when compared to the FRP only 'standard' approach (Model 1). The

545 equivalent RMSE reductions seen for Model 3 were lower, but still significant (-37±12%, -37±7%, and -17±6%, respectively). These results provide evidence that complementary FRP and K-line data could be used widely to improve fire emissions estimation, not only for the gases tested here but also for many others since MCE is well correlated to the EF of many species (Bertschi et al., 2003; McMeeking et al., 2009; Urbanski, 2013; Yokelson et al., 1996). Our findings point to the potential for using this method with future spaceborne high spectral resolution data that can map the K-line from space at

the same time as thermal remote sensing is used to retrieve the fires FRP. According to our findings, such complementary data shows for the first time a proven ability to determine sub-pixel fire combustion phase which can provide an ability to significantly improve fire emission estimation. We then demonstrate the value of the most effective approach on airborne remote sensing data of real wildfires, pointing the way to its ultimate application to potentially improving global fire emissions estimation through its application to spaceborne observations.

Data availability

The data supporting this article are openly available from the King's College London research data repository, KORDS, at https://doi.org/10.18742/26826448.

All the data in this study are available from the authors upon request.

Author contributions

FOB: Conceptualization, Methodology, Formal Analysis, Investigation, Writing – Original Draft, Visualization. MW: Conceptualization, Funding acquisition, Writing – Review & Editing, Supervision. MG: Methodology, Writing – Review & Editing. YL: Resources, Writing – Review & Editing.

Competing interests

The contact author has declared that none of the authors have any competing interests.

Acknowledgements

We thank Dr Zixia Liu from King's College London for assisting with the collection techniques for the trace gas measurements in the laboratory. The Leverhulme Centre for Wildfires, Environment and Society and National Centre for Earth Observation (NCEO) are both thanked for their support of this research. We also thank the European Space Agency (ESA) for supporting the featured airborne campaign. NERC British Antarctic Survey (BAS) are thanked for their support in providing and operating the airborne platform used during the campaign, whilst the NERC Airborne Research and Survey

Facility (ARSF), and now the NCEO Airborne Earth Observatory (NAEO) Team of NCEO-King's College London, are thanked for coordinating and delivering the campaign. The UK's NERC Earth Observation Data Acquisition and Analysis Service (NEODAAS) processed the hyperspectral airborne data used herein to a calibrated and co-located Level 1b product. The views in this publication can in no way be taken to reflect the official opinion of the European Space Agency or any other funding body.

Financial support

FOB is supported by a PhD Studentship from the London NERC DTP (grant no. NE/R012148/1). The practical work undertaken in this research was supported by the Leverhulme Centre for Wildfires, Environment and Society through the Leverhulme Trust (grant number RC-2018-023), by NERC National Capability funding to the National Centre for Earth Observation (NCEO, NE/Ro16518/1), and by the European Space Agency project 'Evaluation and Validation of Sentinel-3 Active Fire Detector and FRP Products experiment' (FIDEX; Contract number 4000136760/21/NL/FF/ab).

References

Akagi, S.K., Yokelson, R.J., Wiedinmyer, C., Alvarado, M.J., Reid, J.S., Karl, T., Crounse, J.D., Wennberg, P.O., 2011. Emission factors for open and domestic biomass burning for use in atmospheric models. Atmospheric Chemistry and Physics 11, 4039–4072. https://doi.org/10.5194/acp-11-4039-2011

Amici, S., Wooster, M.J., Piscini, A., 2011. Multi-resolution spectral analysis of wildfire potassium emission signatures using laboratory, airborne and spaceborne remote sensing. Remote Sensing of Environment 115, 1811–1823. https://doi.org/10.1016/j.rse.2011.02.022

Andreae, M.O., 2019. Emission of trace gases and aerosols from biomass burning - An updated assessment. Atmospheric Chemistry and Physics 19, 8523–8546. https://doi.org/10.5194/acp-19-8523-2019

Andreae, M.O., Merlet, P., 2001. Emission of trace gases and aerosols from biomass burning. Global biogeochemical cycles 15, 955–966. https://doi.org/10.1029/2000GB001382

Berk, A., Anderson, G.P., Bernstein, L.S., Acharya, P.K., Dothe, H., Matthew, M.W., Adler-Golden, S.M., Chetwynd, Jr., J.H., Richtsmeier, S.C., Pukall, B., Allred, C.L., Jeong, L.S., Hoke, M.L., 1999. MODTRAN4 radiative transfer modeling for atmospheric correction, in: Larar, A.M. (Ed.), . Presented at the SPIE's International Symposium on Optical Science, Engineering, and Instrumentation, Denver, CO, USA, p. 348. https://doi.org/10.1117/12.366388

Bertschi, I., Yokelson, R.J., Ward, D.E., Babbitt, R.E., Susott, R.A., Goode, J.G., Hao, W.M., 2003. Trace gas and particle emissions from fires in large diameter and belowground biomass fuels. Journal of Geophysical Research: Atmospheres 108. https://doi.org/10.1029/2002jd002100

Burling, I.R., Yokelson, R.J., Akagi, S.K., Urbanski, S.P., Wold, C.E., Griffith, D.W.T., Johnson, T.J., Reardon, J., Weise, D.R., 2011. Airborne and ground-based measurements of the trace gases and particles emitted by prescribed fires in the United States. Atmospheric Chemistry and Physics 11, 12197–12216. https://doi.org/10.5194/acp-11-12197-2011

Burling, I.R., Yokelson, R.J., Griffith, D.W.T., Johnson, T.J., Veres, P., Roberts, J.M., Warneke, C., Urbanski, S.P., Reardon, J., Weise, D.R., Hao, W.M., De Gouw, J., 2010. Laboratory measurements of trace gas emissions from biomass burning of fuel types from the southeastern and southwestern United States. Atmos. Chem. Phys. 10, 11115–11130. https://doi.org/10.5194/acp-10-11115-2010

Chuvieco, E., Mouillot, F., Van Der Werf, G.R., San Miguel, J., Tanase, M., Koutsias, N., García, M., Yebra, M., Padilla, M., Gitas, I., Heil, A., Hawbaker, T.J., Giglio, L., 2019. Historical background and current developments for mapping burned area from satellite Earth observation. Remote Sensing of Environment 225, 45–64. https://doi.org/10.1016/j.rse.2019.02.013

Coheur, P.-F., Clarisse, L., Turquety, S., Hurtmans, D., Clerbaux, C., 2009. IASI measurements of reactive trace species in biomass burning plumes. Atmos. Chem. Phys. 9, 5655–5667. https://doi.org/10.5194/acp-9-5655-2009

Dennison, P.E., Charoensiri, K., Roberts, D.A., Peterson, S.H., Green, R.O., 2006. Wildfire temperature and land cover modeling using hyperspectral data. Remote Sensing of Environment 100, 212–222. https://doi.org/10.1016/j.rse.2005.10.007

Dennison, P.E., Matheson, D.S., 2011. Comparison of fire temperature and fractional area modeled from SWIR, MIR, and TIR multispectral and SWIR hyperspectral airborne data. Remote Sensing of Environment 115, 876–886. https://doi.org/10.1016/j.rse.2010.11.015

620 Dennison, P.E., Roberts, D.A., 2009. Daytime fire detection using airborne hyperspectral data. Remote Sensing of Environment 113, 1646–1657. https://doi.org/10.1016/j.rse.2009.03.010

Dozier, J., 1981. A method for satellite identification of surface temperature fields of subpixel resolution. Remote Sensing of Environment 11, 221–229. https://doi.org/10.1016/0034-4257(81)90021-3

Freeborn, P.H., Wooster, M.J., Hao, W.M., Ryan, C.A., Nordgren, B.L., Baker, S.P., Ichoku, C., 2008. Relationships

625 between energy release, fuel mass loss, and trace gas an aerosol emissions during laboratory biomass fires. Journal of Geophysical Research Atmospheres 113, 1–17. https://doi.org/10.1029/2007JD008679

Garg, P., Wang, S., Oakes, J.M., Bellini, C., Gollner, M.J., 2024. Variations in gaseous and particulate emissions from flaming and smoldering combustion of Douglas fir and lodgepole pine under different fuel moisture conditions. Combustion and Flame 263, 113386. https://doi.org/10.1016/j.combustflame.2024.113386

630 Giglio, L., Justice, C.O., 2003. Effect of wavelength selection on characterization of fire size and temperature. International Journal of Remote Sensing 24, 3515–3520. https://doi.org/10.1080/0143116031000117056

Giglio, L., Kendall, J.D., 2001. Application of the Dozier retrieval to wildfire characterization a sensitivity analysis. Remote Sensing of Environment 77, 34–49. https://doi.org/10.1016/S0034-4257(01)00192-4

Giglio, L., Randerson, J.T., Van Der Werf, G.R., 2013. Analysis of daily, monthly, and annual burned area using the fourth-

635 generation global fire emissions database (GFED4). Journal of Geophysical Research: Biogeosciences 118, 317–328. https://doi.org/10.1002/jgrg.20042

Ichoku, C., Kaufman, Y.J., 2005. A method to derive smoke emission rates from MODIS fire radiative energy measurements. IEEE Trans. Geosci. Remote Sensing 43, 2636–2649. https://doi.org/10.1109/TGRS.2005.857328

Johnston, J.M., Wooster, M.J., Lynham, T.J., 2014. Experimental confirmation of the MWIR and LWIR grey body

640 assumption for vegetation fire flame emissivity. International Journal of Wildland Fire 23, 463–479. https://doi.org/10.1071/WF12197

Kaiser, J.W., Heil, A., Andreae, M.O., Benedetti, A., Chubarova, N., Jones, L., Morcrette, J.-J., Razinger, M., Schultz, M.G., Suttie, M., van der Werf, G.R., 2012. Biomass burning emissions estimated with a global fire assimilation system based on observed fire radiative power. Biogeosciences 9, 527–554. https://doi.org/10.5194/bg-9-527-2012

Kaufman, Y.J., Kleidman, R.G., King, M.D., 1998. SCAR-B fires in the tropics: Properties and remote sensing from EOS-MODIS. J. Geophys. Res. 103, 31955–31968. https://doi.org/10.1029/98JD02460

Lacaux, J.P., Delmas, R., Jambert, C., Kuhlbusch, T.A.J., 1996. NO_x emissions from African savanna fires. J. Geophys. Res. 101, 23585–23595. https://doi.org/10.1029/96JD01624

Magidimisha, E., Griffith, D.J., 2017. Remote optical observations of actively burning biomass fires using potassium line spectral emission. Fourth Conference on Sensors, MEMS, and Electro-Optic Systems 10036, 1003611–1003611. https://doi.org/10.1117/12.2244284

Magidimisha, E., Naidoo, S., Faniso-Mnyaka, Z., Nana, M.A., Naidoo, S.V., Skosana, V., 2023. A UAV Based System for Real-Time Near-Infrared Monitoring of Small-Scale Wildfires. International Journal on Advances in Software.

Matheson, D.S., Dennison, P.E., 2012. Evaluating the effects of spatial resolution on hyperspectral fire detection and temperature retrieval. Remote Sensing of Environment 124, 780–792. https://doi.org/10.1016/j.rse.2012.06.026

McMeeking, G.R., Kreidenweis, S.M., Baker, S., Carrico, C.M., Chow, J.C., Collett, J.L., Hao, W.M., Holden, A.S., Kirchstetter, T.W., Malm, W.C., Moosmüller, H., Sullivan, A.P., Wold, C.E., 2009. Emissions of trace gases and aerosols during the open combustion of biomass in the laboratory. J. Geophys. Res. 114, D19210. https://doi.org/10.1029/2009JD011836

Mebust, A.K., Cohen, R.C., 2013. Observations of a seasonal cycle in NO_x emissions from fires in African woody savannas. Geophysical Research Letters 40, 1451–1455. https://doi.org/10.1002/grl.50343

Mota, B., Wooster, M.J., 2018. A new top-down approach for directly estimating biomass burning emissions and fuel consumption rates and totals from geostationary satellite fire radiative power (FRP). Remote Sensing of Environment 206, 45–62. https://doi.org/10.1016/j.rse.2017.12.016

665   Nguyen, H.M., He, J., Wooster, M.J., 2023. Biomass burning CO, PM and fuel consumption per unit burned area estimates derived across Africa using geostationary SEVIRI fire radiative power and Sentinel-5P CO data. Atmos. Chem. Phys. 23, 2089–2118. https://doi.org/10.5194/acp-23-2089-2023

Nguyen, H.M., Wooster, M.J., 2020. Advances in the estimation of high Spatio-temporal resolution pan-African top-down biomass burning emissions made using geostationary fire radiative power (FRP) and MAIAC aerosol optical depth

670   (AOD) data. Remote Sensing of Environment 248, 111971–111971. https://doi.org/10.1016/j.rse.2020.111971

Owsley-Brown, F. Dataset used in 'Can remote sensing combustion phase improve estimates of landscape fire smoke emission rate and composition?' (AMT-2024-73). KORDS. https://doi.org/10.18742/26826448

Rabelo, E.R.C., Veras, C.A.G., Carvalho, J.A., Alvarado, E.C., Sandberg, D.V., Santos, J.C., 2004. Log smoldering after an

675   amazonian deforestation fire. Atmospheric Environment 38, 203–211. https://doi.org/10.1016/j.atmosenv.2003.09.065

Reid, J.S., Eck, T.F., Christopher, S.A., Koppman, R., Dubovik, O., Eleuterio, D.P., Holben, B.N., Reid, E.A., Zhang, J., 2005. A review of biomass burning emissions part II: Intensive optical properties of biomass burning particles. Atmospheric Chemistry and Physics 5, 827–849. https://doi.org/10.5194/acp-5-827-2005

680   Reid, J.S., Hobbs, P.V., 1998. Physical and optical properties of young smoke from individual biomass fires in Brazil. J. Geophys. Res. 103, 32013–32030. https://doi.org/10.1029/98JD00159

Reisen, F., Meyer, C.P., Weston, C.J., Volkova, L., 2018. Ground-Based Field Measurements of PM2.5 Emission Factors From Flaming and Smoldering Combustion in Eucalypt Forests. Journal of Geophysical Research: Atmospheres 123, 8301–8314. https://doi.org/10.1029/2018JD028488

685   Ross, A.N., Wooster, M.J., Boesch, H., Parker, R., 2013. First satellite measurements of carbon dioxide and methane emission ratios in wildfire plumes: GOSAT MEASURE OF CO_2:CH_4 EMISSION RATIO. Geophys. Res. Lett. 40, 4098–4102. https://doi.org/10.1002/grl.50733

Urbanski, S., 2014. Wildland fire emissions, carbon, and climate: Emission factors. Forest Ecology and Management 317, 51–60. https://doi.org/10.1016/j.foreco.2013.05.045

690   Urbanski, S.P., 2013. Combustion efficiency and emission factors for wildfire-season fires in mixed conifer forests of the
            northern Rocky Mountains, US. Atmos. Chem. Phys. 13, 7241–7262. https://doi.org/10.5194/acp-13-7241-2013

        Vernooij, R., Eames, T., Russell-Smith, J., Yates, C., Beatty, R., Evans, J., Edwards, A., Ribeiro, N., Wooster, M., Strydom,
            T., Giongo, M.V., Borges, M.A., Menezes Costa, M., Barradas, A.C.S., Van Wees, D., Van Der Werf, G.R., 2023.
            Dynamic savanna burning emission factors based on satellite data using a machine learning approach. Earth Syst.
695   Dynam. 14, 1039–1064. https://doi.org/10.5194/esd-14-1039-2023

        Vernooij, R., Winiger, P., Wooster, M., Strydom, T., Poulain, L., Dusek, U., Grosvenor, M., Roberts, G.J., Schutgens, N.,
            Van Der Werf, G.R., 2022. A quadcopter unmanned aerial system (UAS)-based methodology for measuring
            biomass burning emission factors. Atmos. Meas. Tech. 15, 4271–4294. https://doi.org/10.5194/amt-15-4271-2022

        Vodacek, A., Kremens, R.L., Fordham, A.J., Vangorden, S.C., Luisi, D., Schott, J.R., Latham, D.J., 2002. Remote optical
700   detection of biomass burning using a potassium emission signature. International Journal of Remote Sensing 23,
            2721–2726. https://doi.org/10.1080/01431160110109633

        Waigl, C.F., Prakash, A., Stuefer, M., Verbyla, D., Dennison, P., 2019. Fire detection and temperature retrieval using EO-1
            Hyperion data over selected Alaskan boreal forest fires. International Journal of Applied Earth Observation and
            Geoinformation 81, 72–84. https://doi.org/10.1016/j.jag.2019.03.004

705   Ward, D.E., Radke, L.F., 1993. Emissions Measurements from Vegetation Fires : A Comparative Evaluation of Methods and
            Results, Fire in the Environment: The Ecological, Atmospheric, and Climatic Importance of Vegetation Fires,
            edited by: Crutzen, P. J. and Goldammer, J. G., JohnWiley, New York 53–76.

        Wiedinmyer, C., Akagi, S.K., Yokelson, R.J., Emmons, L.K., Al-Saadi, J.A., Orlando, J.J., Soja, A.J., 2011. The Fire
            INventory from NCAR (FINN): a high resolution global model to estimate the emissions from open burning.
710   Geosci. Model Dev. 17.

        Wooster, M.J., Freeborn, P.H., Archibald, S., Oppenheimer, C., Roberts, G.J., Smith, T.E.L., Govender, N., Burton, M.,
            Palumbo, I., 2011. Field determination of biomass burning emission ratios and factors via open-path FTIR
            spectroscopy and fire radiative power assessment: Headfire, backfire and residual smouldering combustion in

African savannahs. Atmospheric Chemistry and Physics 11, 11591–11615. https://doi.org/10.5194/acp-11-11591-2011

Wooster, M.J., Roberts, G., Perry, G.L.W., Kaufman, Y.J., 2005. Retrieval of biomass combustion rates and totals from fire radiative power observations: FRP derivation and calibration relationships between biomass consumption and fire radiative energy release. Journal of Geophysical Research Atmospheres 110, 1–24. https://doi.org/10.1029/2005JD006318

Wooster, M.J., Roberts, G.J., Giglio, L., Roy, D.P., Freeborn, P.H., Boschetti, L., Justice, C., Ichoku, C., Schroeder, W., Davies, D., Smith, A.M.S., Setzer, A., Csiszar, I., Strydom, T., Frost, P., Zhang, T., Xu, W., de Jong, M.C., Johnston, J.M., Ellison, L., Vadrevu, K., Sparks, A.M., Nguyen, H., McCarty, J., Tanpipat, V., Schmidt, C., San-Miguel-Ayanz, J., 2021. Satellite remote sensing of active fires: History and current status, applications and future requirements. Remote Sensing of Environment 267, 112694. https://doi.org/10.1016/j.rse.2021.112694

Yokelson, R.J., Andreae, M.O., Akagi, S.K., 2013. Pitfalls with the use of enhancement ratios or normalized excess mixing ratios measured in plumes to characterize pollution sources and aging. Atmospheric Measurement Techniques 6, 2155–2158. https://doi.org/10.5194/amt-6-2155-2013

Yokelson, R.J., Griffith, D.W.T., Ward, D.E., 1996. Open-path fourier transform infrared studies of large-scale laboratory biomass fires. Journal of Geophysical Research Atmospheres 101, 21067–21080. https://doi.org/10.1029/96jd01800

Yokelson, R.J., Susott, R., Ward, D.E., Reardon, J., Griffith, D.W.T., 1997. Emissions from smoldering combustion of biomass measured by open-path Fourier transform infrared spectroscopy. J. Geophys. Res. 102, 18865–18877. https://doi.org/10.1029/97JD00852

Zhang, T., Wooster, M., Green, D.C., Main, B., 2020. A Mathematical Approach to Merging Data from Different Trace Gas/Particulate Sensors Having Dissimilar (T90) Response Times: Application to Fire Emission Factor Determination. Aerosol Air Qual. Res. 20, 281–290. https://doi.org/10.4209/aaqr.2019.02.0061

Zhang, T., Wooster, M.J., Green, D.C., Main, B., 2015. New field-based agricultural biomass burning trace gas, PM 2.5 , and black carbon emission ratios and factors measured in situ at crop residue fires in Eastern China. Atmospheric Environment 121, 22–34. https://doi.org/10.1016/j.atmosenv.2015.05.010

Zheng, B., Chevallier, F., Ciais, P., Yin, Y., Wang, Y., 2018. On the Role of the Flaming to Smoldering Transition in the

740   Seasonal   Cycle   of   African   Fire   Emissions.   Geophys.   Res.   Lett.   45,   11,998-12,007. https://doi.org/10.1029/2018GL079092

Zhukov, B., Lorenz, E., Oertel, D., Wooster, M., Roberts, G., 2006. Spaceborne detection and characterization of fires during the bi-spectral infrared detection (BIRD) experimental small satellite mission (2001–2004). Remote Sensing of Environment 100, 29–51. https://doi.org/10.1016/j.rse.2005.09.019

745 **Appendices**

Appendix A – spectral -fitting model

Reducing the modelled spectra to a single thermal component for the fire resulted in far poorer fits than with two components, particularly at shorter wavelengths, and increasing the number of thermal components delivered results having negligible fractional area and thus no detectable improvement in the modelled spectra. Thus, two fire thermal

750 components were seen as the optimum choice – and allowed a high-quality fit to the measured spectra and a strong ability to estimate total FRP, but the retrieved fire temperatures could not be used to reliably estimate extent of flaming and smoldering activity.

Appendix B – alternative approaches going via combustion rate

As detailed in Section 1, most conventional remote sensing approaches to estimating fire emissions rely on first estimating

755 the fuel mass burned. Therefore, FAM and FAD approaches involving this step were also tested as an alternative to the more direct approaches evaluated in Section 4.4. Combustion rate (gs^{-1}) was determined by first estimating total carbon flux (Figure 5d) in moles and multiplying this by 12 $gmol^{-1}$, the resulting figure agreeing well with the mass loss obtained from the scales data. Both emission factors and relationships between FRP and combustion rate were calculated for the four combustion types: fire-average, flaming-dominated, flaming-identified and smouldering. Models analogous to FAM

760 and FAD were then tested. These estimated combustion rate, which was then multiplied by emission factors to give

emission rates. These were then compared to the measured rates. The results were almost identical to those presented in Section 4.5 as the methods are also identical, except for the step of converting to combustion rate. This method did, however, indicate that the relationship between measured FRP and rate of combustion was different between the two combustion phases.

765